Characterizing Mars' magnetotail topology with respect to the upstream interplanetary magnetic fields

Shaosui Xu[1], David L. Mitchell[1], Tristan Weber[2], David A. Brain[2], Janet G. Luhmann[1], Chuanfei Dong[3], Shannon M. Curry[1], Yingjuan Ma[4], Gina A. DiBraccio[5], Jasper Halekas[6], Yaxue Dong[2], Christian Mazelle[7]

[1]Space Sciences Laboratory, University of California, Berkeley, CA, USA
[2]Laboratory for Atmospheric and Space Physics, University of Colorado, Boulder, CO, USA
[3]Department of Astrophysical Sciences and Princeton Plasma Physics Laboratory, Princeton University, Princeton, NJ, USA
[4]Department of Earth and Space Sciences, University of California, Los Angeles, CA, USA
[5]NASA Goddard Space Flight Center, Greenbelt, MD, USA
[6]Department of Physics and Astronomy, University of Iowa, Iowa City, IA, USA
[7]IRAP, CNRS - University of Toulouse - UPS - CNES, Toulouse, France

Key Points:

- This study provides a detailed mapping of tail magnetic topology at Mars, which is dominated by draped and open magnetic field lines
- Both the MHD model and data show significant changes in Martian tail topology with respect to east/west IMFs
- It implies that Mars' crustal fields have a global effect on the magnetosphere configuration, supporting the picture of a hybrid magnetotail

Corresponding author: Shaosui Xu, shaosui.xu@ssl.berkeley.edu

Abstract

The canonical picture of the magnetotail of unmagnetized planets consists of draped interplanetary magnetic fields (IMF) forming opposite-directed lobes, separated by the current sheet. *DiBraccio et al.* [2018] showed that Mars' magnetotail has a twist departing from this picture. Magnetohydrodynamic (MHD) results suggest that open field lines connected to the planet that populate portions of the tail cause the apparent twist. To validate this interpretation, we compare the tail topology determined from MHD simulations to that inferred from data collected by the Mars Atmosphere and Volatile EvolutioN (MAVEN) spacecraft, in particular how each topology responds to the upstream IMF orientation. The occurrence rates for open topology from both data and MHD varies with IMF polarities in a similar fashion as the tail twisting. This suggests that Mars' crustal fields have a global effect on the magnetosphere configuration, supporting the picture of a "hybrid" magnetotail that is partly induced/draped and partly intrinsic/planetary in origin.

1 Introduction

Venus and Mars both lack an intrinsic global dipole magnetic field but have a significant ionosphere mainly produced by solar extreme ultraviolet photons ionizing the neutral atmosphere, and thus share many similarities in terms of their interaction with the solar wind. Both have an induced magnetosphere formed with the upstream IMF being piled up and draped around the planet. A prominent difference between these two planets is that Mars possesses localized strong crustal magnetic fields [e.g. *Acuna et al.*, 1999; *Connerney et al.*, 2005] that contribute to and modify its induced magnetosphere features on a global scale [e.g. *Brain et al.*, 2007] while Venus has a negligible intrinsic dipole magnetic field at the current epoch [e.g. *Phillips and Russell*, 1987]. As a result, Venus' induced magnetotail consists of two magnetic lobes with oppositely directed magnetic fields formed by draped IMF, separated by a current sheet perpendicular to the plane of the IMF and the solar wind flow [e.g. *Saunders and Russell*, 1986; *Luhmann*, 1986; *McComas et al.*, 1986; *Zhang et al.*, 2010], as illustrated in the left column of Figure 1.

In contrast, Mars' magnetotail departs from this canonical induced-tail picture, having an apparent inter-lobe current sheet twist away from the expected $+/-\mathbf{E_{conv}}$ location, as reported by *DiBraccio et al.* [2018], also shown in the right column of Figure 1. This twist also varies depending on the IMF sector (hereafter referred as east and west, corresponding to Parker spiral fields pointing away from and toward the sun, as well as $B_y > 0$

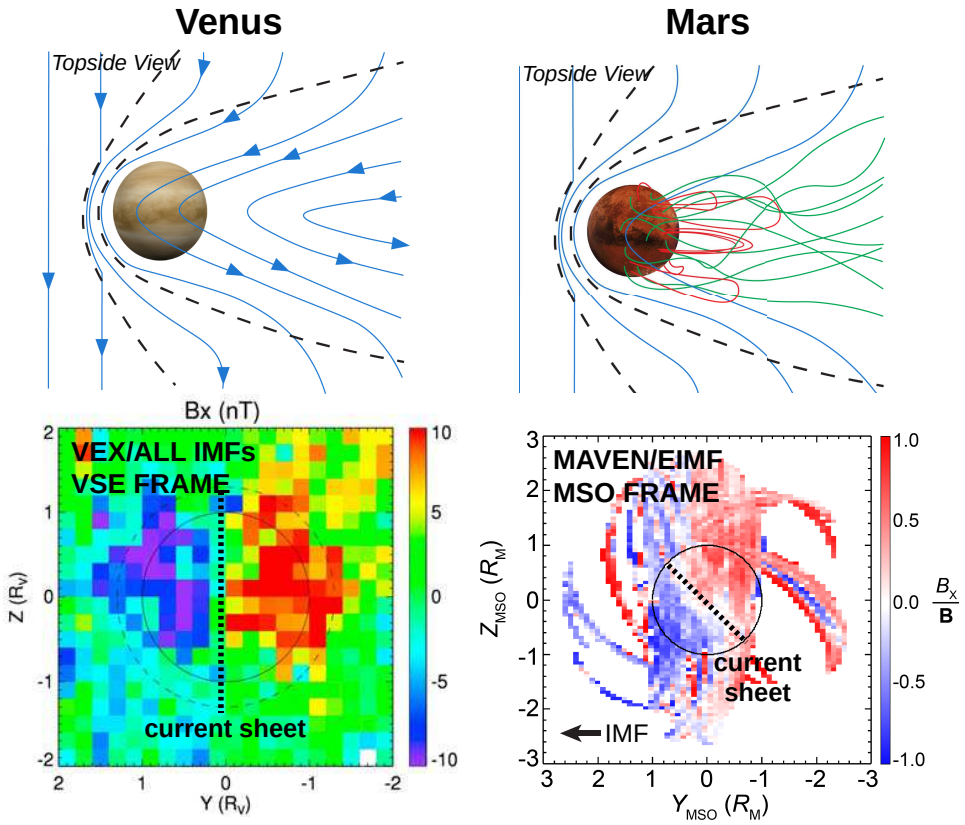

Figure 1. The comparison of the Venus' (the left column) and Mars' magnetotails (the right column). The top two panels are schematics of the tail configuration and magnetic topologies and the bottom two panels are the averaged B_x in the tail from measurements by Venus Express and MAVEN, (adopted from Figure 2 of *Zhang et al.* [2010] and Figure 2 of *DiBraccio et al.* [2018]), respectively. The dotted black lines in the bottom panels indicate the current sheet that separates the two lobes. The lower left panel is for all IMF directions under the Venus Solar Electric coordinates (VSE) such that the X-axis is antiparallel to the solar wind flow, the Z-axis aligned with the convection electric field ($\mathbf{E_{conv}} = -\mathbf{V} \times \mathbf{B}$), and the Y-axis completing the right-handed system. The lower right panel is in the Mars-centered Solar Orbital (MSO) frame for east IMFs only. In the MSO frame, the X axis points from the center of Mars to the Sun, the Z axis points to the north pole of Mars' elliptical orbit plane, and the Y axis completes the right-handed system.

and $B_y < 0$, respectively), suggesting Mars' crustal magnetic fields play a role. *DiBraccio et al.* [2018] further compared the tail configuration from MHD with or without crustal magnetic fields included and revealed that the tail twist was indeed attributed to the inclusion of crustal magnetic fields. They proposed that Mars' magnetotail is part of a hybrid magnetosphere, consisting of a global intrinsic dipole field (from the low-order dipole

term of the crustal magnetism) contribution surrounded by induced/draped fields [*Dubinin et al.*, 1980, 1994].

Mars' crustal magnetic fields can magnetically reconnect with the IMF [e.g. *Harada et al.*, 2017, 2018], giving rise to complex and dynamic magnetic topologies [e.g. *Brain et al.*, 2007; *Lillis and Brain*, 2013; *Xu et al.*, 2018a, 2019a; *Weber et al.*, 2019]. Magnetic topology consists of closed (both of the footpoints of a magnetic field line connected to the planet), open (one footpoint of a field line connected to the planet and the other to the solar wind), and draped (both of the footpoints of a field line connected back to the solar wind). Mars' magnetotail consists of various magnetic topologies, instead of simply draped like Venus, as reported by previous studies. Nightside tail topology at low altitudes has been studied in detail with Mars Global Surveyor (MGS) data [*Brain et al.*, 2007] and MAVEN data [*Weber et al.*, 2017]. Photoelectrons have been observed in the tail by both the Mars Express (MEx) spacecraft [*Frahm et al.*, 2006, 2010; *Coates et al.*, 2011] and MAVEN [*Xu et al.*, 2016a, 2017a,b], interpreted as magnetic connectivity to the dayside ionosphere through open field lines [*Liemohn et al.*, 2006] or closed field lines [*Xu et al.*, 2016a, 2017b]. *Luhmann et al.* [2015a] analyzed magnetic topology from MHD simulations and found that a significant portion of Mars' magnetotail is populated with open field lines.

The magnetotail topology is also important for characterizing electron precipitation [e.g. *Fillingim et al.*, 2007; *Němec et al.*, 2010; *Lillis et al.*, 2011; *Shane et al.*, 2016; *Adams et al.*, 2018] and low-energy ion escape [e.g. *Fränz et al.*, 2015; *Dubinin et al.*, 2017; *Inui et al.*, 2018]. Solar wind electrons can precipitate along open field lines, and ionospheric photoelectrons along cross-terminator closed field lines onto the (nightside) atmosphere, causing ionization and auroral emission. Meanwhile, low-energy ions can escape along open field lines [e.g. *Ergun et al.*, 2015; *Jakosky et al.*, 2018], partly driven by ambipolar electric fields [e.g. *Collinson et al.*, 2015; *Ergun et al.*, 2016; *Xu et al.*, 2018b; *Akbari et al.*, 2019], and on draped field lines, mainly accelerated by the $\mathbf{J} \times \mathbf{B}$ force and/or the convection electric field [e.g. *Fang et al.*, 2008; *Dong et al.*, 2014; *Halekas et al.*, 2017a; *Cravens et al.*, 2017]. More general properties of the Martian magnetotail are discussed in several review papers [*Nagy et al.*, 2004; *Bertucci et al.*, 2011; *Dubinin and Fraenz*, 2015; *Liemohn and Xu*, 2018].

DiBraccio et al. [2018] advocated for the key role of the crustal fields in introducing the twist to Mars' magnetotail with MAVEN magnetic field data and modeling efforts. To further validate the picture of a hybrid Martian magnetotail, we compare the actual tail topology determined from the MHD simulations with topology inferred from the MAVEN superthermal electron data, in particular, how each magnetic topology varies with respect to the upstream IMF polarity. The results of this study on the detailed characterization of the tail topology are also important for understanding the energy and particle exchange between Mars' ionosphere and the solar wind.

2 Methodology

To infer magnetic topology from the MAVEN data, we utilize a new technique developed by *Xu et al.* [2019b] that combines superthermal electrons' energy and pitch angle distributions. This technique mainly relies on three basic principals: (1) the presence of photoelectrons in one or both field-aligned directions indicates the magnetic field line has one or both footpoint(s) embedded in the *dayside* ionosphere at the superthermal electron exobase (~160 km, [*Xu et al.*, 2016b]); (2) the presence of loss cones in one or both field-aligned directions indicates the magnetic field line has one or both footpoint(s) embedded in the collisional atmosphere; (3) the presence of superthermal electron voids indicates both footpoints of the magnetic field line are connected to the nightside atmosphere [*Mitchell et al.*, 2001; *Steckiewicz et al.*, 2015]. Magnetic topology is determined based on where each end of the field line is inferred to connect. One caveat of inferring magnetic topology from electrons is that we can only determine field lines' connectivity to the ionosphere but not to the planet's surface so that deeply draped field lines can be identified as "open" topology. Photoelectrons can be identified automatically with a shape parameter [*Xu et al.*, 2017a], loss cones with a PAD score [*Weber et al.*, 2017], and electron voids by the electron flux level. The detailed description of how to combine all these aspects to infer magnetic topology is provided in *Xu et al.* [2019b]. In this study, we analyze magnetic topology from December 2014 to September 2018, based on the superthermal electron measurements by the Solar Wind Electron Analyzer (SWEA) instrument [*Mitchell et al.*, 2016] and magnetic field vector measurements by the magnetometer (MAG) instrument [*Connerney et al.*, 2015] onboard MAVEN .

When the MAVEN orbit samples the upstream solar wind, we obtain the IMF clock angle, $\tan^{-1}(Bz/By)$ in the MSO frame, directly from MAG measurements in that region

[*Halekas et al.*, 2015, 2017b]. Otherwise, we use a proxy based on MAG measurements in the sheath [*Dong et al.*, 2019]. Thus, each pass through the tail has IMF clock angle estimates both before and after. We then assign each inferred magnetic topology within the magnetosphere with an upstream IMF clock angle by interpolating between the inbound and outbound values.

We determine the occurrence rate of the model magnetic topology from 16 steady-state simulations with the multi-species 3-D MHD model [*Ma et al.*, 2002, 2004]. Nominal Parker spiral IMFs and a nominal solar wind proton density (4 cm^{-3}) and speed (400 km/s) with the fall equinox condition are used. Eight simulations are generated for the east IMF ($B_y > 0$) and eight for the west IMF ($B_y < 0$) in the MSO frame. For each IMF direction, the eight simulations consist of the neutral atmospheres and ionization frequencies for the solar maximum and minimum conditions as well as four subsolar longitudes (SSL) for when the southern strong crustal magnetic fields are located on the dayside (SSL = 180°), dawn (SSL = 90°), dusk (SSL = 270°), and nightside (SSL = 0°). For each simulation, magnetic field line tracing starts from a grid of points in the $Y - Z$ plane at $X = -2\ R_M$. Magnetic topology for each field line is determined from its connectivity to at 150 km altitude and/or a radial distance of 3 R_M, where R_M is the Mars radius. The occurrence rate is calculated as the fraction of each magnetic topology type in the respective tail grid for the eight simulations in each IMF sector, i.e. each grid point has eight samples of topology. We note that the models provide steady state "snapshots" of the Mars field topology, which in reality is constantly changing as Mars rotates [*Ma et al.*, 2014].

3 Results

3.1 Data-Model Comparison

As illustrated in the lower right panel of Figure 1, as well as Figure 2 of *DiBraccio et al.* [2018], Mars' magneotail has a twist in its lobes and current sheet. MHD results show that this twist also has topological signatures. We take the tail topology from MHD at $X_{MSO} = -2\ R_M$ under the east IMF condition as an example, shown in Figure 2a. The tail field topology from MHD consists of draped field lines (blue) in the outmost layer, surrounding mostly open field lines connected to the dayside (green with black dots overplotted), and then open field lines connected to the nightside (green). There is also a

central region of closed field lines (red) whose size varies with down-tail distance. This topology ordering is the same for the other 15 MHD simulations, but varying in exact locations. A case for the west IMF is shown in Figure S1b in the supplementary material.

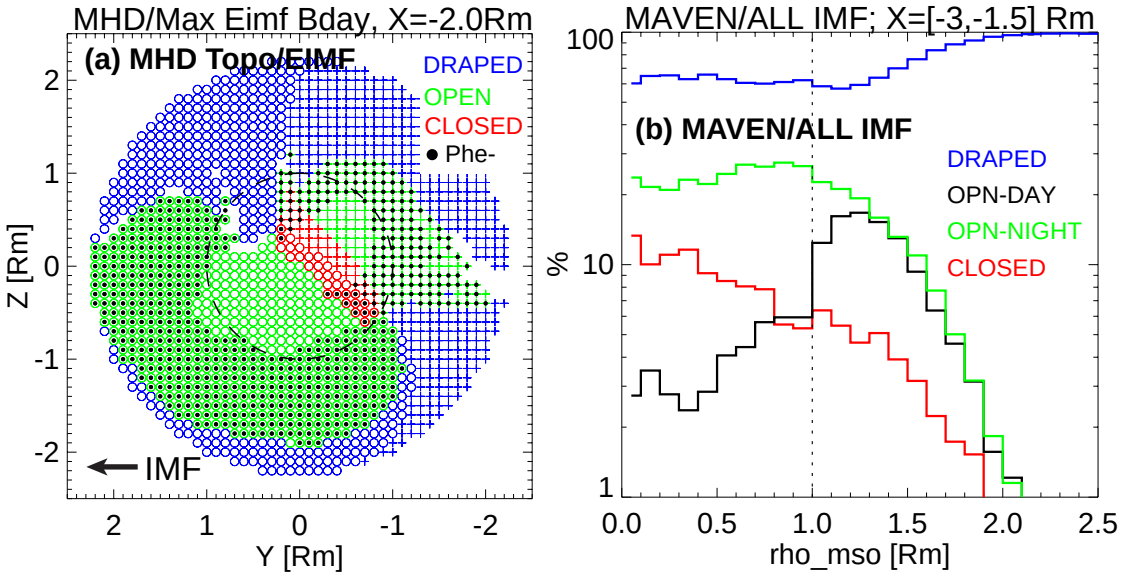

Figure 2. (a) Magnetic topology from MHD at $X_{MSO} = -2\ R_M$ for an east upstream IMF and strong crustal fields located on the dayside (SSL=180°), blue for draped, green for open, and red for closed, with black dots indicating field lines connected back to dayside. Circles are for $B_x < 0$ and '+' for $B_x > 0$. (b) The cylindrical averaged occurrence rates of magnetic topologies in the tail ($X_{MSO} = [-1.5, -3]\ R_M$) from MAVEN data for all IMFs as a function of $\rho_{MSO} = \sqrt{Y_{MSO}^2 + Z_{MSO}^2}$, blue for draped, black for open-to-day, green for open-to-night, and red for closed.

The magnetic topology inferred from MAVEN data shows a similar ordering, in the sense of the dominant spatial location for each topology. Figure 2b shows the cylindrically averaged occurrence rates of magnetic topologies for all IMFs against $\rho_{MSO} = \sqrt{Y_{MSO}^2 + Z_{MSO}^2}$. We take a cylindrical averaging because the occurrence rates are roughly cylindrical symmetric (as shown in Figures S1c-S1f in the supplementary material). The data results show that draped fields occur over 80% of the time for $\rho > 1.5\ R_M$, open-to-day fields are mostly concentrated at $1 < \rho < 1.5\ R_M$, open-to-night fields occur most frequently within the optical shadow, and the occurrence rates for closed fields peak at 10% at the center. This ordering of where each topology occurs most frequently agree with MHD results.

To examine how the IMF polarity affects the tail topology for both MHD and the data, we compare occurrence rates for the east and west IMF separately. The occurrence rates from the data have been averaged over all planetary rotations, and over a range of EUV flux and solar wind conditions. To better capture the twist, we limit our analysis to data with an upstream IMF clock angle less than 30° or greater than 150° so that the IMF is mostly in the $X_{MSO} - Y_{MSO}$ plane. In addition, we rotate the frame such that the Y-axis is parallel or antiparallel to the Y component of the upstream IMF for east and west IMF sectors, respectively, with X still pointing at the Sun and Z completing the right-handed system. To approximate this with the MHD simulations, we average the topology in two groups of eight models (4 SSLs × 2 solar conditions for east and west IMF separately). The comparison is shown in Figure 3. The color range is 0 to 1 for MHD results (left column) but 0 to 0.5 for MAVEN results (right column), as the occurrence rates from MHD are roughly twice that of MAVEN data. We use different color ranges to highlight relative variations in the occurrence rates. Because the sampling of the model averages is different from the sampling of the data, and because of some limitations of the MHD model (discussed later), we do not expect detailed agreement. Instead, we use the models to guide our interpretation.

Although the overall occurrence rates from the model and data differ significantly, the patterns of the occurrence rates and their variation with respect to IMF polarities share similarities. For east IMF (the top row), the open topology occurs most frequently in the $+Z/-Y$ and $-Z/+Y$ quadrants in both simulations and data, in agreement with the orientation of the current sheet for this IMF direction as shown in Figure 2 of *DiBraccio et al.* [2018]. Some differences between the model and data are expected since the model is from a thin slice at $X = -2\ R_M$ whereas the data are averaged over slice with a thickness of 1.5 R_M. For west IMF (bottom row), open topology occurs most frequently in the $+Z/+Y$ quadrant in both simulations and data but only simulations show a significant region of open topology in the $-Z/-Y$ quadrant. Again, these topological results are in agreement with a $\sim 90°$ rotation of the current sheet about the X axis when the IMF polarity changes from east to west*DiBraccio et al.* [2018].

The occurrence rates for draped topology from MHD and data are shown in Figure 4, separated for east and west upstream IMFs. The occurrence rate for draped topology in the data is mostly above 50% whereas the open topology shown in Figure 3 has an occurrence rate below 50%. In contrast, the probability for draped topology from MHD

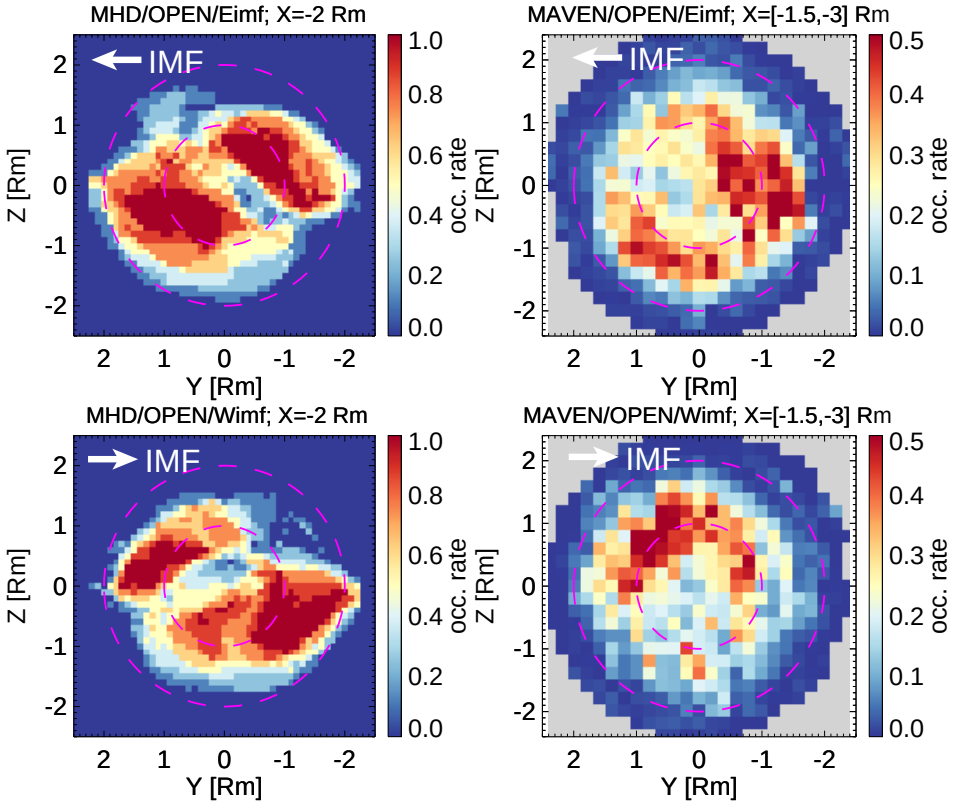

Figure 3. Model-data comparison for open topology for east (top row) and west IMF (bottom row). The left column shows the occurrence rates from MHD at $X_{MSO} = -2\ R_M$, calculated from eight simulations (four SSLs and two solar conditions) separately for each and west IMFs, and right from MAVEN data for $X_{MSO} = [-1.5, -3]\ R_M$. Note that the color ranges for the occurrence rates from MHD (the left column) and data (the right column) are different to highlight features.

reaches down to nearly 0 within the two tail lobes, where open topology prevails instead. Furthermore, MHD predicts a higher occurrence rate of closed field lines near the current sheet, which is not present in the data (not shown).

In summary, the discrepancies between results from the MAVEN data and MHD modeling include: (a) a factor of two difference in the maximum occurrence rates for the open topology, (b) occurrence rates in the $-Y/-Z$ quadrant and (c) occurrence rates for closed field lines. We can identify three possible causes for these differences. First, the multi-species MHD model relies on numerical diffusion, as a substitute for magnetic diffusion, to enable magnetic reconnection. It is not known how well this approach approximates the actual rate of magnetic reconnection. An artificially high reconnection rate

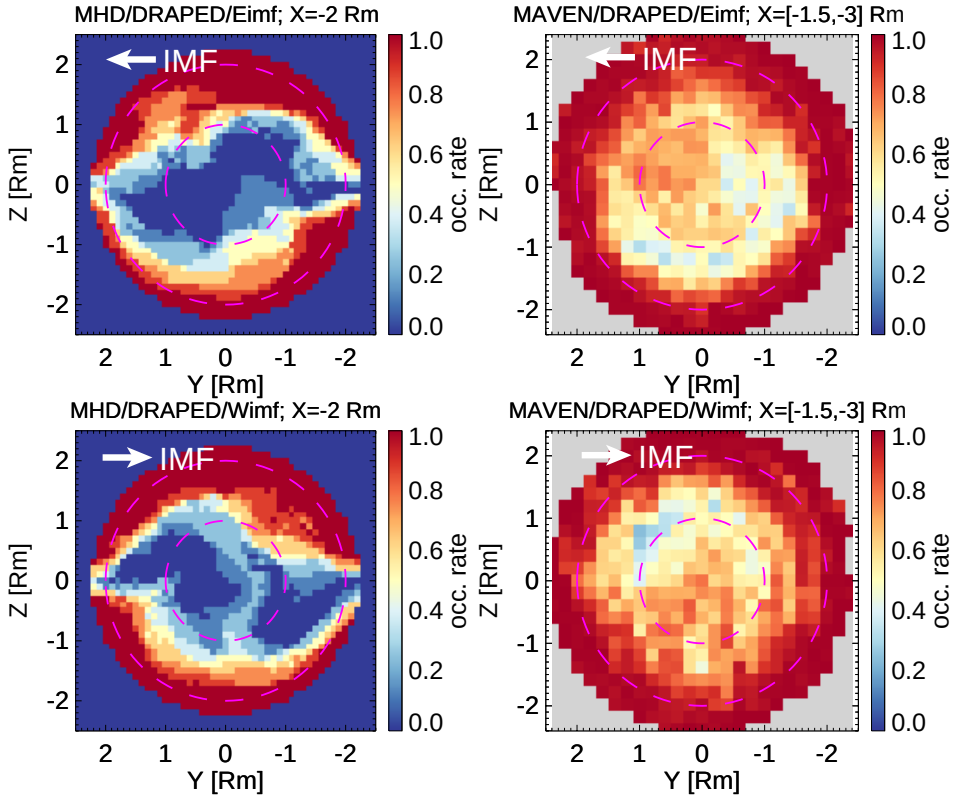

Figure 4. Model-data comparison for draped topology for east (top row) and west IMF (bottom row). The same format as Figure 3 but for draped topology. The left column shows the occurrence rates from MHD at $X_{MSO} = -2\ R_M$ and right from MAVEN data $X_{MSO} = [-1.5, -3]\ R_M$.

would result in more open/closed field lines. Second, the occurrence rate from MHD is calculated based on only eight steady-state simulations for each IMF polarity, which might not accurately reflect the actual sampling of data over different seasons and continuously rotating crustal field orientations. Third, SWEA has an angular resolution of $\sim 20°$, which might be insufficient to resolve small loss/source cones, expected to be smaller than $< 10°$ over strongly magnetized regions of the crust. This might result in an underestimation of open field lines associated with strong crustal fields in the south.

3.2 Open Topology in the Tail

The results above suggest that the presence of a high occurrence rate of open topology significantly impacts the Martian magnetotail configuration. It also has important implications for characterizing cold ion outflow and electron precipitation. In Figure 5, we

show the occurrence rates for the open topology in the $X_{MSO} - R_{MSO}$ projection, where $R_{MSO} = \frac{Z_{MSO}}{|Z_{MSO}|}\sqrt{Y_{MSO}^2 + Z_{MSO}^2}$.

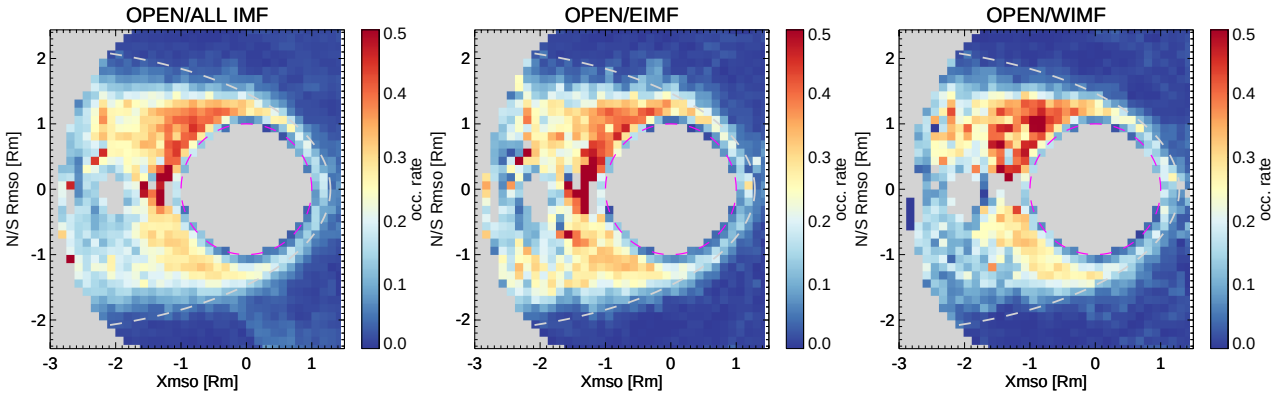

Figure 5. Occurrence rates of open topology in the $X_{MSO} - R_{MSO}$ projection for all MAVEN data (left), east (middle), and west IMF (right), respectively. The white dashed lines are conic fits of the induced magnetic boundary from *Vignes et al.* [2000].

Overall, the occurrence rate of the open topology mostly ranges from 20% to 50% on the nightside, decreasing further down the tail. There is a north-south asymmetry in Figure 5, with a higher occurrence rate in the north, regardless of the upstream IMF polarity, as the twist in the tail topology is averaged out for each hemisphere. This north-south asymmetry probably occurs because: (1) cusps of open field lines consist of a small spatial area/solid angle over the southern strong crustal fields; (2) more deeply draped field lines (into the collisional atmosphere) in the north hemisphere identified as open field lines by our technique; and (3) we underestimate the occurrence rate over strong crustal fields due to SWEA's angular resolution. One noticeable difference is that the occurrence rate for $R_{MSO} < 0$ and $X < -1.5\ R_M$ is higher for east IMFs (middle) than west IMFs (right). Two possible explanations are: (1) the strong crustal fields in the south magnetically reconnect more with the east IMF; (2) the solar wind flow in the tail has a component preferentially in the opposite direction from the convection electric field, to conserve momentum after picking up planetary ions, and might push magnetic field lines towards $-\mathbf{E}_{\mathbf{conv}}$, which is $-Z_{MSO}$ for east IMFs but $+Z_{MSO}$ for west IMFs, an effect suggested by *Chai et al.* [2019].

4 Discussion and Conclusions

Motivated by the evidence that the apparent twist of the Martian magnetotail is caused by reconnection between the IMF and the crustal fields [*DiBraccio et al.*, 2018], we compare magnetic topology inferred from the MAVEN data with that from MHD simulations. From both the model and data, Mars' magnetotail is found to be dominated by combinations of draped and open magnetic topologies, and not merely draped IMFs as at Venus. In addition, the pattern of open field lines in the tail at $X =\sim -2\ R_M$ downstream varies significantly with the dominant IMF sectors in both data and simulations, in agreement with the tail polarity pattern (e.g. cross-tail current sheet) twisting in opposite directions in response to the different IMFs. These results are consistent with the interpretation that the large portion of open field lines populating the tail produces the twist.

One might argue that magnetic topology inferred from superthermal electrons cannot distinguish deeply draped IMF below the electron exobase from field lines connected to the surface, so that some field lines identified as open by our technique may in fact be deeply draped. However, the variation in occurrence rates of open field lines in response to changes in the IMF polarity supports the interpretation that Mars' crustal magnetic fields cause the tail twist, because the conditions for magnetic reconnection between IMF and crustal magnetic fields depend on IMF polarity. These same conditions also affect where the draped IMF can penetrate deeply into the ionosphere.

This tail topology variation with the IMF polarity also echoes draped field distortions revealed by *Brain et al.* [2006] with MGS observations: the magnetic field at 400-km altitude over a northern weak crustal region is more consistent with a draping pattern under the west IMF but more scattered in directions under the east IMF. *Luhmann et al.* [2015b] showed from MHD simulations that this distortion is likely due to different reconnection geometries for different IMF polarities. While the results from *Brain et al.* [2006] are for dayside, open field lines from dayside magnetic reconnection will populate part of the tail lobes, forming at least part of the open-to-day topology seen in the tail. In all, previous studies and our results suggest that the Martian crustal magnetic fields have a global effect on the magnetosphere configuration, supporting the picture of a hybrid magnetotail at Mars.

Acknowledgments

The MAVEN project is supported by NASA through the Mars Exploration Program. The MAVEN data used in this study are available through Planetary Data System (https://pds-ppi.igpp.ucla.edu/mission/MAVEN). The BATS-R-US code is publicly available from http://csem.engin.umich.edu/tools/swmf. S. Xu gratefully acknowledges the artistic skills of Jessica Still and the time she dedicated to create the schematics presented in Figure 1.

References

Acuna, M., J. Connerney, R. Lin, D. Mitchell, C. Carlson, J. McFadden, K. Anderson, H. Rème, C. Mazelle, D. Vignes, et al. (1999), Global distribution of crustal magnetization discovered by the Mars Global Surveyor MAG/ER experiment, *Science*, *284*(5415), 790–793.

Adams, D., S. Xu, D. L. Mitchell, R. L. Lillis, M. Fillingim, L. Andersson, C. Fowler, J. E. P. Connerney, J. Espley, and C. Mazelle (2018), Using Magnetic Topology to Probe the Sources of Mars' Nightside Ionosphere, *Geophysical Research Letters*, *0*(ja), doi:10.1029/2018GL080629.

Akbari, H., L. Andersson, W. Peterson, J. Espley, M. Benna, and R. Ergun (2019), Ambipolar Electric Field in the Martian Ionosphere: MAVEN Measurements, *Journal of Geophysical Research: Space Physics*, *124*(6), 4518–4524.

Bertucci, C., F. Duru, N. Edberg, M. Fraenz, C. Martinecz, K. Szego, and O. Vaisberg (2011), The induced magnetospheres of mars, venus, and titan, *Space science reviews*, *162*(1-4), 113–171.

Brain, D., R. Lillis, D. Mitchell, J. Halekas, and R. Lin (2007), Electron pitch angle distributions as indicators of magnetic field topology near Mars, *Journal of Geophysical Research: Space Physics (1978–2012)*, *112*(A9).

Brain, D. A., D. L. Mitchell, and J. S. Halekas (2006), The magnetic field draping direction at Mars from April 1999 through August 2004, *Icarus*, *182*(2), 464–473.

Chai, L., W. Wan, Y. Wei, T. Zhang, W. Exner, M. Fraenz, E. Dubinin, M. Feyerabend, U. Motschmann, Y. Ma, et al. (2019), The Induced Global Looping Magnetic Field on Mars, *The Astrophysical Journal Letters*, *871*(2), L27.

Coates, A. J., S. Tsang, A. Wellbrock, R. Frahm, J. Winningham, S. Barabash, R. Lundin, D. Young, and F. Crary (2011), Ionospheric photoelectrons: Comparing Venus, Earth, Mars and Titan, *Planetary and Space Science*, *59*(10), 1019–1027.

Collinson, G., D. Mitchell, A. Glocer, J. Grebowsky, W. K. Peterson, J. Connerney, L. Andersson, J. Espley, C. Mazelle, J.-A. Sauvaud, A. Fedorov, Y. Ma, S. Bougher, R. Lillis, R. Ergun, and B. Jakosky (2015), Electric Mars: The first direct measurement of an upper limit for the Martian "polar wind" electric potential, *Geophysical Research Letters*, *42*(21), 9128–9134, doi:10.1002/2015GL065084, 2015GL065084.

Connerney, J., M. Acuña, N. Ness, G. Kletetschka, D. Mitchell, R. Lin, and H. Reme (2005), Tectonic implications of Mars crustal magnetism, *Proceedings of the national*

Academy of Sciences of the United States of America, *102*(42), 14,970–14,975.

Connerney, J., J. Espley, P. Lawton, S. Murphy, J. Odom, R. Oliversen, and D. Sheppard (2015), The MAVEN magnetic field investigation, *Space Science Reviews*, pp. 1–35.

Cravens, T. E., O. Hamil, S. Houston, S. Bougher, Y. Ma, D. Brain, and S. Ledvina (2017), Estimates of ionospheric transport and ion loss at mars, *Journal of Geophysical Research: Space Physics*, *122*(10), 10,626–10,637, doi:10.1002/2017JA024582.

DiBraccio, G. A., J. G. Luhmann, S. M. Curry, J. R. Espley, S. Xu, D. L. Mitchell, Y. Ma, C. Dong, J. R. Gruesbeck, J. E. P. Connerney, Y. Harada, S. Ruhunusiri, J. S. Halekas, Y. Soobiah, T. Hara, D. A. Brain, and B. M. Jakosky (2018), The Twisted Configuration of the Martian Magnetotail: MAVEN Observations, *Geophysical Research Letters*, *45*(10), 4559–4568, doi:10.1029/2018GL077251.

Dong, C., S. W. Bougher, Y. Ma, G. Toth, A. F. Nagy, and D. Najib (2014), Solar wind interaction with Mars upper atmosphere: Results from the one-way coupling between the multifluid MHD model and the MTGCM model, *Geophysical Research Letters*, *41*, 2708–2715, doi:10.1002/2014GL059515.

Dong, Y., X. Fang, D. Brain, D. Hurley, J. Halekas, J. Espley, R. Ramstad, S. Ruhunusiri, and B. Jakosky (2019), Magnetic field in the Martian magnetosheath and the application as an IMF clock angle proxy, *Journal of Geophysical Research: Space Physics*.

Dubinin, E., and M. Fraenz (2015), Magnetotails of mars and venus, in *Magnetotails in the solar system*, vol. 207, pp. 34–59, John Wiley Hoboken, NJ.

Dubinin, E., R. Lundin, and K. Schwingenschuh (1994), Solar wind electrons as tracers of the martian magnetotail topology, *Journal of Geophysical Research: Space Physics*, *99*(A11), 21,233–21,240.

Dubinin, E., M. Fraenz, M. Pätzold, J. McFadden, J. Halekas, G. DiBraccio, J. Connerney, F. Eparvier, D. Brain, B. Jakosky, et al. (2017), The effect of solar wind variations on the escape of oxygen ions from Mars through different channels: MAVEN observations, *Journal of Geophysical Research: Space Physics*, *122*(11), 11–285.

Dubinin, E. M., P. Izrailevich, and I. Podgornyi (1980), The combined magnetosphere, *Kosmicheskie Issledovaniia*, *18*, 470–474.

Ergun, R. E., M. W. Morooka, L. A. Andersson, C. M. Fowler, G. T. Delory, D. J. Andrews, A. I. Eriksson, T. McEnulty, and B. M. Jakosky (2015), Dayside electron temperature and density profiles at mars: First results from the maven langmuir probe and waves instrument, *Geophysical Research Letters*, *42*(21), 8846–8853, doi:

366 10.1002/2015GL065280.

367 Ergun, R. E., L. A. Andersson, C. M. Fowler, A. K. Woodson, T. D. Weber, G. T. Delory,
368 D. J. Andrews, A. I. Eriksson, T. McEnulty, M. W. Morooka, A. I. F. Stewart, P. Ma-
369 haffy, and B. M. Jakosky (2016), Enhanced o2+ loss at mars due to an ambipolar elec-
370 tric field from electron heating, *Journal of Geophysical Research: Space Physics*, *121*(5),
371 4668–4678, doi:10.1002/2016JA022349.

372 Fang, X., M. W. Liemohn, A. F. Nagy, Y. Ma, D. L. De Zeeuw, J. U. Kozyra, and T. H.
373 Zurbuchen (2008), Pickup oxygen ion velocity space and spatial distribution around
374 Mars, *Journal of Geophysical Research: Space Physics*, *113*(A2).

375 Fillingim, M. O., L. M. Peticolas, R. J. Lillis, D. A. Brain, J. S. Halekas, D. L. Mitchell,
376 R. P. Lin, D. Lummerzheim, S. W. Bougher, and D. L. Kirchner (2007), Model calcu-
377 lations of electron precipitation induced ionization patches on the nightside of Mars,
378 *Geophysical Research Letters*, *34*, L12101, doi:10.1029/2007GL029986.

379 Frahm, R., J. Sharber, J. Winningham, P. Wurz, M. Liemohn, E. Kallio, M. Yamauchi,
380 R. Lundin, S. Barabash, A. Coates, et al. (2006), Locations of atmospheric photoelec-
381 tron energy peaks within the Mars environment, *Space Science Reviews*, *126*(1-4), 389–
382 402.

383 Frahm, R., J. Sharber, J. Winningham, R. Link, M. Liemohn, J. Kozyra, A. Coates,
384 D. Linder, S. Barabash, R. Lundin, et al. (2010), Estimation of the escape of photo-
385 electrons from Mars in 2004 liberated by the ionization of carbon dioxide and atomic
386 oxygen, *Icarus*, *206*(1), 50–63.

387 Fränz, M., E. Dubinin, D. Andrews, S. Barabash, H. Nilsson, and A. Fedorov (2015),
388 Cold ion escape from the Martian ionosphere, *Planetary and Space Science*, *119*, 92–
389 102.

390 Halekas, J., E. Taylor, G. Dalton, G. Johnson, D. Curtis, J. McFadden, D. Mitchell,
391 R. Lin, and B. Jakosky (2015), The solar wind ion analyzer for MAVEN, *Space Science*
392 *Reviews*, *195*(1-4), 125–151.

393 Halekas, J., D. Brain, J. Luhmann, G. DiBraccio, S. Ruhunusiri, Y. Harada, C. Fowler,
394 D. Mitchell, J. Connerney, J. Espley, et al. (2017a), Flows, Fields, and Forces in the
395 Mars-Solar Wind Interaction, *Journal of Geophysical Research: Space Physics*, *122*(11).

396 Halekas, J., S. Ruhunusiri, Y. Harada, G. Collinson, D. Mitchell, C. Mazelle, J. McFad-
397 den, J. Connerney, J. Espley, F. Eparvier, et al. (2017b), Structure, dynamics, and sea-
398 sonal variability of the Mars-solar wind interaction: MAVEN Solar Wind Ion Ana-

399 lyzer in-flight performance and science results, *Journal of Geophysical Research: Space*
400 *Physics*, *122*(1), 547–578.

401 Harada, Y., J. Halekas, J. McFadden, J. Espley, G. DiBraccio, D. Mitchell, C. Mazelle,
402 D. Brain, L. Andersson, Y. Ma, et al. (2017), Survey of magnetic reconnection signa-
403 tures in the Martian magnetotail with MAVEN, *Journal of Geophysical Research: Space*
404 *Physics*.

405 Harada, Y., J. S. Halekas, G. A. DiBraccio, S. Xu, J. Espley, J. P. Mcfadden, D. L.
406 Mitchell, C. Mazelle, D. A. Brain, T. Hara, Y. J. Ma, S. Ruhunusiri, and B. M.
407 Jakosky (2018), Magnetic Reconnection on Dayside Crustal Magnetic Fields at
408 Mars: MAVEN Observations, *Geophysical Research Letters*, *45*(10), 4550–4558, doi:
409 10.1002/2018GL077281.

410 Inui, S., K. Seki, S. Sakai, D. Brain, T. Hara, J. McFadden, J. Halekas, D. Mitchell,
411 G. DiBraccio, and B. Jakosky (2018), Statistical Study of Heavy Ion Outflows From
412 Mars Observed in the Martian-Induced Magnetotail by MAVEN, *Journal of Geophysical*
413 *Research: Space Physics*.

414 Jakosky, B., D. Brain, M. Chaffin, S. Curry, J. Deighan, J. Grebowsky, J. Halekas,
415 F. Leblanc, R. Lillis, J. Luhmann, et al. (2018), Loss of the Martian atmosphere to
416 space: Present-day loss rates determined from MAVEN observations and integrated loss
417 through time, *Icarus*, *315*, 146 – 157, doi:https://doi.org/10.1016/j.icarus.2018.05.030.

418 Liemohn, M. W., and S. Xu (2018), Recent advances regarding the mars magnetotail cur-
419 rent sheet, *Electric Currents in Geospace and Beyond*, *235*, 177.

420 Liemohn, M. W., Y. Ma, R. A. Frahm, X. Fang, J. U. Kozyra, A. F. Nagy, J. D. Winning-
421 ham, J. R. Sharber, S. Barabash, and R. Lundin (2006), Mars Global MHD Predictions
422 of Magnetic Connectivity Between the Dayside Ionosphere and the Magnetospheric
423 Flanks, *Space Science Reviews*, *126*, 63–76, doi:10.1007/s11214-006-9116-8.

424 Lillis, R. J., and D. A. Brain (2013), Nightside electron precipitation at Mars: Geographic
425 variability and dependence on solar wind conditions, *Journal of Geophysical Research:*
426 *Space Physics*, *118*(6), 3546–3556.

427 Lillis, R. J., M. O. Fillingim, and D. A. Brain (2011), Three-dimensional structure of
428 the Martian nightside ionosphere: Predicted rates of impact ionization from Mars
429 Global Surveyor magnetometer and electron reflectometer measurements of precipi-
430 tating electrons, *Journal of Geophysical Research (Space Physics)*, *116*(A15), A12317,
431 doi:10.1029/2011JA016982.

Luhmann, J. (1986), The solar wind interaction with Venus, *Space science reviews*, *44*(3-4), 241–306.

Luhmann, J., C. Dong, Y. Ma, S. Curry, D. Mitchell, J. Espley, J. Connerney, J. Halekas, D. Brain, B. Jakosky, et al. (2015a), Implications of MAVEN Mars near-wake measurements and models, *Geophysical Research Letters*, *42*(21), 9087–9094.

Luhmann, J., Y.-J. Ma, D. Brain, D. Ulusen, R. Lillis, J. Halekas, and J. Espley (2015b), Solar wind interaction effects on the magnetic fields around Mars: Consequences for interplanetary and crustal field measurements, *Planetary and Space Science*, *117*, 15–23.

Ma, Y., A. F. Nagy, K. C. Hansen, D. L. DeZeeuw, T. I. Gombosi, and K. Powell (2002), Three-dimensional multispecies MHD studies of the solar wind interaction with Mars in the presence of crustal fields, *Journal of Geophysical Research: Space Physics (1978–2012)*, *107*(A10), 1282–1289.

Ma, Y., A. F. Nagy, I. V. Sokolov, and K. C. Hansen (2004), Three-dimensional, multispecies, high spatial resolution MHD studies of the solar wind interaction with Mars, *Journal of Geophysical Research: Space Physics (1978–2012)*, *109*(A7).

Ma, Y., X. Fang, C. T. Russell, A. F. Nagy, G. Toth, J. G. Luhmann, D. A. Brain, and C. Dong (2014), Effects of crustal field rotation on the solar wind plasma interaction with Mars, *Geophysical Research Letters*, *41*(19), 6563–6569.

McComas, D. J., H. E. Spence, C. Russell, and M. Saunders (1986), The average magnetic field draping and consistent plasma properties of the Venus magnetotail, *Journal of Geophysical Research: Space Physics*, *91*(A7), 7939–7953.

Mitchell, D., R. Lin, C. Mazelle, H. Reme, P. Cloutier, J. Connerney, M. Acuña, and N. Ness (2001), Probing Mars' crustal magnetic field and ionosphere with the MGS Electron Reflectometer, *Journal of Geophysical Research: Planets (1991–2012)*, *106*(E10), 23,419–23,427.

Mitchell, D., C. Mazelle, J.-A. Sauvaud, J.-J. Thocaven, J. Rouzaud, A. Fedorov, P. Rouger, D. Toublanc, E. Taylor, D. Gordon, et al. (2016), The MAVEN solar wind electron analyzer, *Space Science Reviews*, *200*(1-4), 495–528.

Nagy, A., D. Winterhalter, K. Sauer, T. Cravens, S. Brecht, C. Mazelle, D. Crider, E. Kallio, A. Zakharov, E. Dubinin, et al. (2004), The plasma environment of Mars, in *Mars? Magnetism and Its Interaction with the Solar Wind*, pp. 33–114, Springer.

Němec, F., D. Morgan, D. Gurnett, and F. Duru (2010), Nightside ionosphere of Mars: Radar soundings by the Mars Express spacecraft, *Journal of Geophysical Research:*

Planets (1991–2012), *115*(E12).

Phillips, J., and C. Russell (1987), Revised upper limit on the internal magnetic moment of Venus, *Advances in space research*, *7*(12), 291–294.

Saunders, M., and C. Russell (1986), Average dimension and magnetic structure of the distant Venus magnetotail, *Journal of Geophysical Research: Space Physics*, *91*(A5), 5589–5604.

Shane, A. D., S. Xu, M. W. Liemohn, and D. L. Mitchell (2016), Mars nightside electrons over strong crustal fields, *Journal of Geophysical Research: Space Physics*, *121*(4), 3808–3823.

Steckiewicz, M., C. Mazelle, P. Garnier, N. Andr. Penou, A. Beth, J.-A. Sauvaud, D. Toublanc, D. L. Mitchell, J. P. McFadden, J. G. Luhmann, R. J. Lillis, J. E. P. Connerney, J. R. Espley, L. Andersson, J. S. Halekas, D. E. Larson, and B. M. Jakosky (2015), Altitude dependence of nightside Martian suprathermal electron depletions as revealed by MAVEN observations, *Geophysical Research Letters*, pp. 8877–8884, doi: 10.1002/2015GL065257, 2015GL065257.

Vignes, D., C. Mazelle, H. Rme, M. H. Acuña, J. E. P. Connerney, R. P. Lin, D. L. Mitchell, P. Cloutier, D. H. Crider, and N. F. Ness (2000), The solar wind interaction with Mars: Locations and shapes of the bow shock and the magnetic pile-up boundary from the observations of the MAG/ER Experiment onboard Mars Global Surveyor, *Geophysical Research Letters*, *27*, 49–52, doi:10.1029/1999GL010703.

Weber, T., D. Brain, D. Mitchell, S. Xu, J. Connerney, and J. Halekas (2017), Characterization of Low-Altitude Nightside Martian Magnetic Topology Using Electron Pitch Angle Distributions, *Journal of Geophysical Research: Space Physics*, *122*(10), 9777–9789, doi:10.1002/2017JA024491, 2017JA024491.

Weber, T., D. Brain, D. Mitchell, S. Xu, J. Espley, J. Halekas, R. Lillis, and B. Jakosky (2019), The Influence of Solar Wind Pressure on Martian Crustal Magnetic Field Topology, *Geophysical Research Letters*, *46*(5), 2347–2354.

Xu, S., D. Mitchell, M. Liemohn, C. Dong, S. Bougher, M. Fillingim, R. Lillis, J. McFadden, C. Mazelle, J. Connerney, and B. Jakosky (2016a), Deep nightside photoelectron observations by MAVEN SWEA: Implications for Martian northern hemispheric magnetic topology and nightside ionosphere source, *Geophysical Research Letters*, *43*(17), 8876–8884, doi:10.1002/2016GL070527, 2016GL070527.

Xu, S., M. Liemohn, S. Bougher, and D. Mitchell (2016b), Martian high-altitude photoelectrons independent of solar zenith angle, *Journal of Geophysical Research: Space Physics*, *121*(4), 3767–3780, doi:10.1002/2015JA022149, 2015JA022149.

Xu, S., D. Mitchell, M. Liemohn, X. Fang, Y. Ma, J. Luhmann, D. Brain, M. Steckiewicz, C. Mazelle, J. Connerney, and B. Jakosky (2017a), Martian low-altitude magnetic topology deduced from MAVEN/SWEA observations, *Journal of Geophysical Research: Space Physics*, *122*(2), 1831–1852, doi:10.1002/2016JA023467, 2016JA023467.

Xu, S., D. Mitchell, J. Luhmann, Y. Ma, X. Fang, Y. Harada, T. Hara, D. Brain, T. Webber, C. Mazelle, and G. A. DiBraccio (2017b), High-altitude closed magnetic loops at Mars observed by MAVEN, *Geophysical Research Letters*, *44*(22), 11,229–11,238, doi:10.1002/2017GL075831, 2017GL075831.

Xu, S., X. Fang, D. L. Mitchell, Y. Ma, J. G. Luhmann, G. A. DiBraccio, T. Weber, D. Brain, C. Mazelle, S. M. Curry, and C. O. Lee (2018a), Investigation of Martian Magnetic Topology Response to 2017 September ICME, *Geophysical Research Letters*, *45*(15), 7337–7346, doi:10.1029/2018GL077708.

Xu, S., D. L. Mitchell, J. P. McFadden, G. Collinson, Y. Harada, R. Lillis, C. Mazelle, and J. E. P. Connerney (2018b), Field-aligned potentials at mars from maven observations, *Geophysical Research Letters*, *45*(19), 10,119–10,127, doi:10.1029/2018GL080136.

Xu, S., S. M. Curry, D. L. Mitchell, J. G. Luhmann, R. J. Lillis, and C. Dong (2019a), Magnetic topology response to the 2003 Halloween ICME event at Mars, *Journal of Geophysical Research: Space Physics*, *124*(1), 151–165.

Xu, S., T. Weber, D. L. Mitchell, D. A. Brain, C. Mazelle, G. A. DiBraccio, and J. Espley (2019b), A technique to infer magnetic topology at Mars and its application to the terminator region, *Journal of Geophysical Research: Space Physics*, *124*(3), 1823–1842.

Zhang, T., W. Baumjohann, J. Du, R. Nakamura, R. Jarvinen, E. Kallio, A. Du, M. Balikhin, J. Luhmann, and C. Russell (2010), Hemispheric asymmetry of the magnetic field wrapping pattern in the Venusian magnetotail, *Geophysical Research Letters*, *37*(14).

Figure 1.

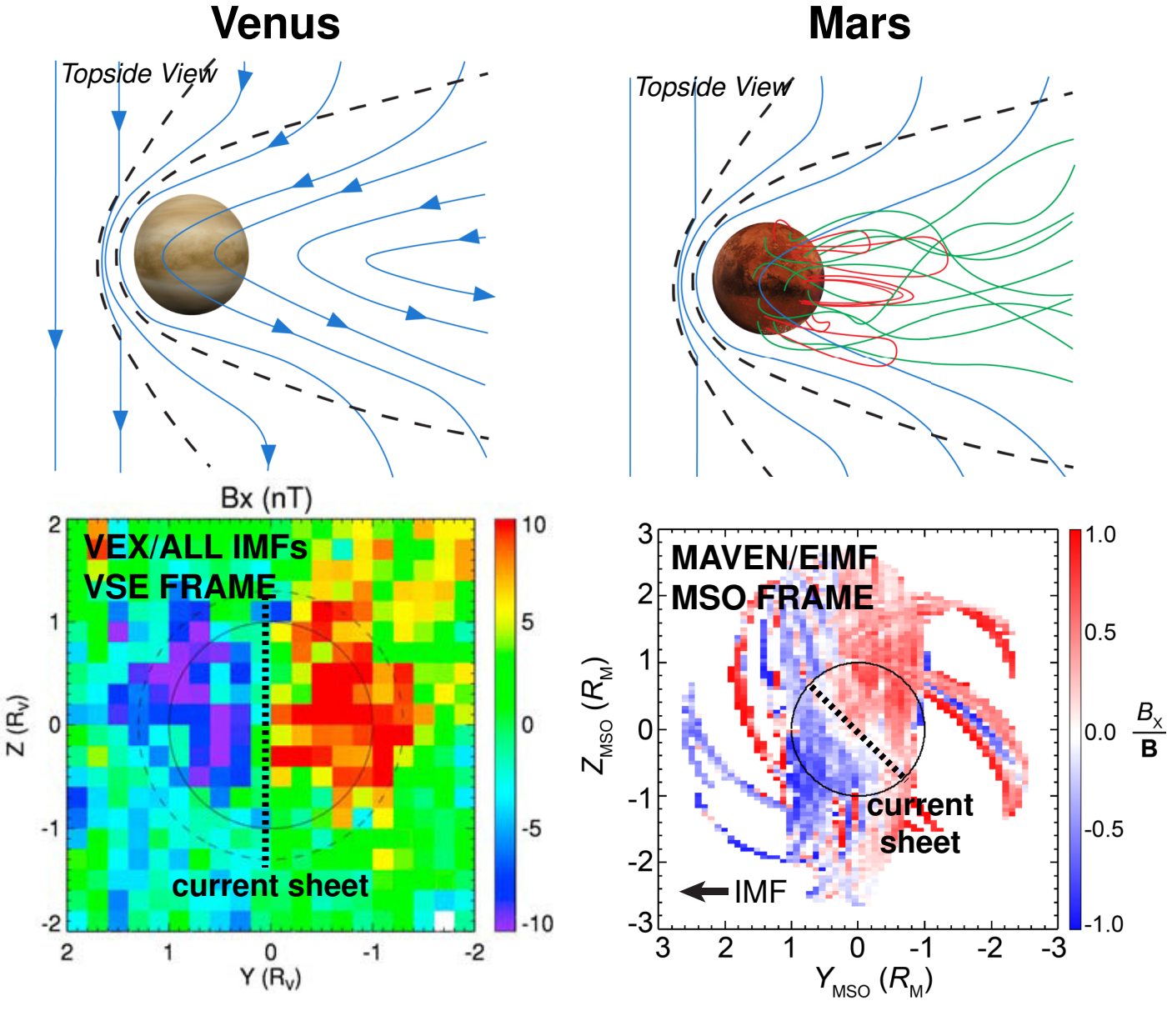
Venus
Topside View
Mars
Topside View
Bx (nT)
VEX/ALL IMFs
VSE FRAME
current sheet
Z (R_V)
Y (R_V)
MAVEN/EIMF
MSO FRAME
current
sheet
IMF
Z_MSO (R_M)
Y_MSO (R_M)
B_X / B

Figure 2.

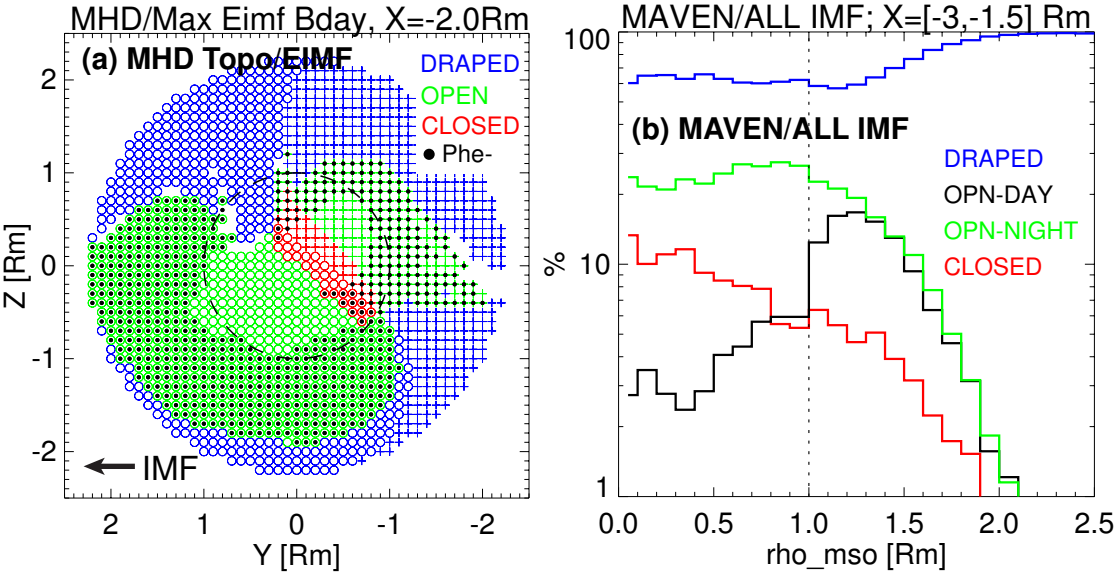
MHD/Max Eimf Bday, X=-2.0Rm
(a) MHD Topo/EIMF
DRAPED
OPEN
CLOSED
Phe-
IMF
Z [Rm]
Y [Rm]
MAVEN/ALL IMF; X=[-3,-1.5] Rm
(b) MAVEN/ALL IMF
DRAPED
OPN-DAY
OPN-NIGHT
CLOSED
%
rho_mso [Rm]

Figure 3.

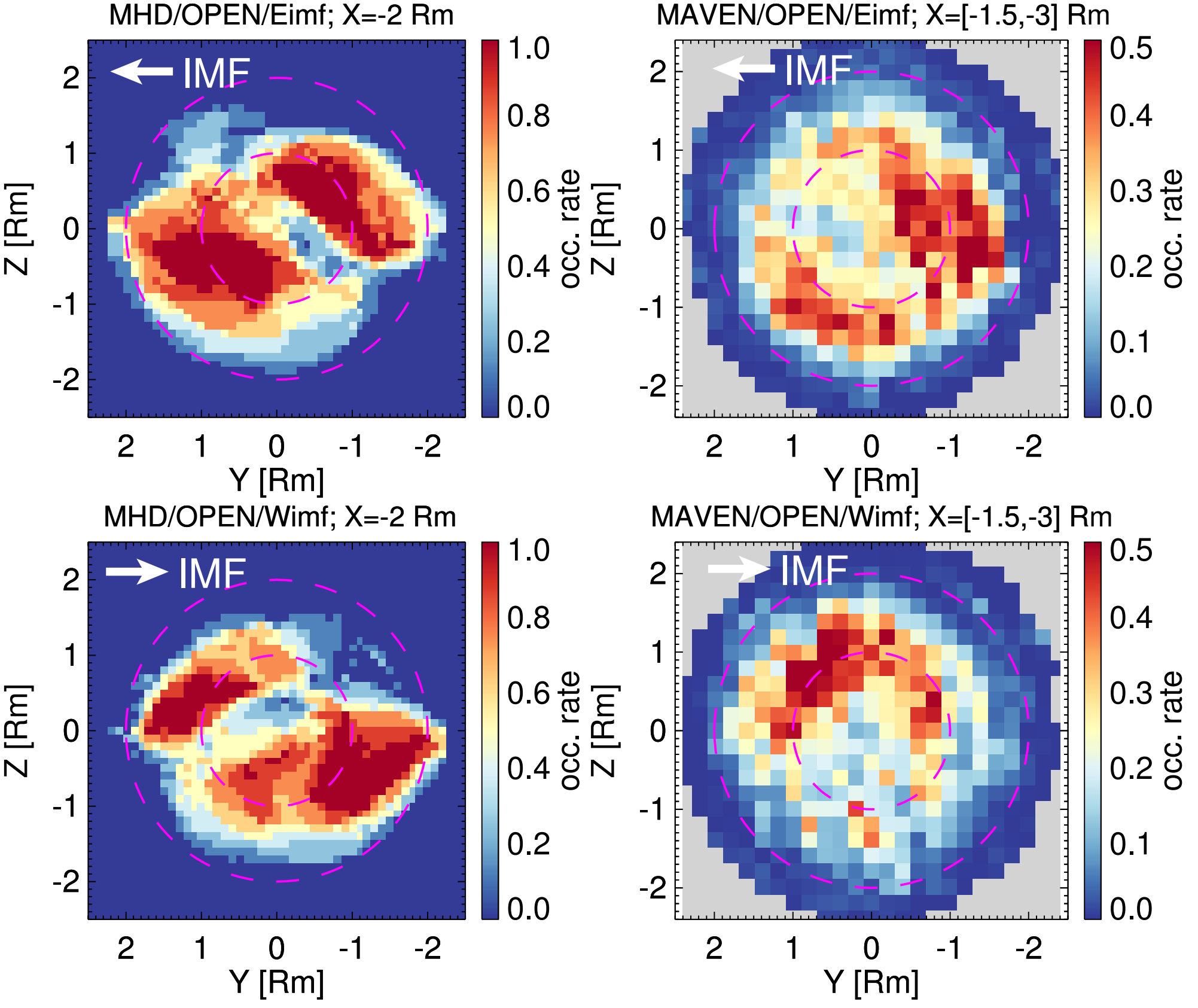
MHD/OPEN/Eimf; X=-2 Rm
MAVEN/OPEN/Eimf; X=[-1.5,-3] Rm
MHD/OPEN/Wimf; X=-2 Rm
MAVEN/OPEN/Wimf; X=[-1.5,-3] Rm
IMF
Z [Rm]
Y [Rm]
occ. rate
2
1
0
-1
-2
1.0
0.8
0.6
0.4
0.2
0.0
0.5
0.4
0.3
0.2
0.1
0.0

Figure 4.

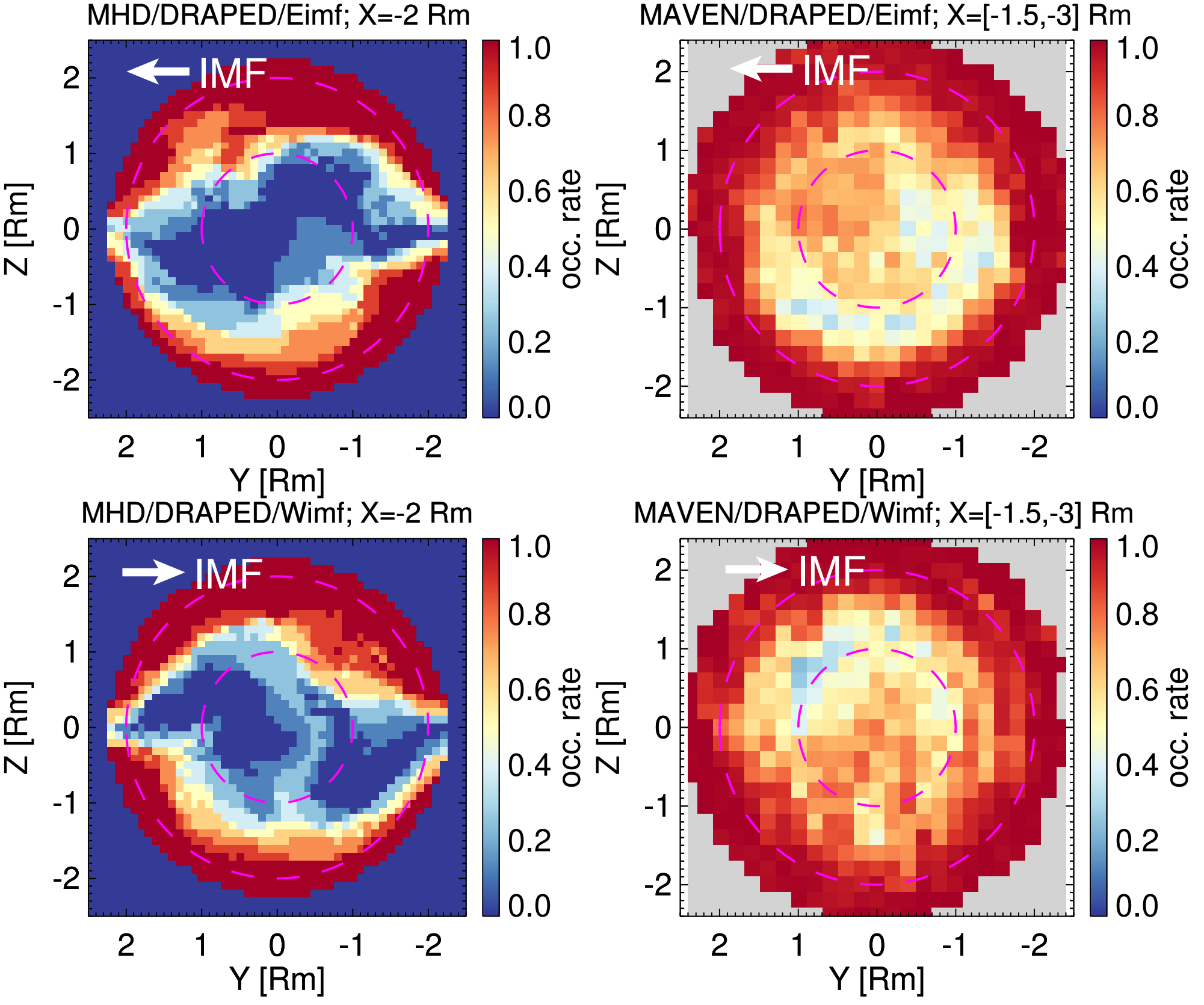
MHD/DRAPED/Eimf; X=-2 Rm
MAVEN/DRAPED/Eimf; X=[-1.5,-3] Rm
MHD/DRAPED/Wimf; X=-2 Rm
MAVEN/DRAPED/Wimf; X=[-1.5,-3] Rm
IMF
Z [Rm]
Y [Rm]
occ. rate
2
1
0
-1
-2
0.0
0.2
0.4
0.6
0.8
1.0

Figure 5.

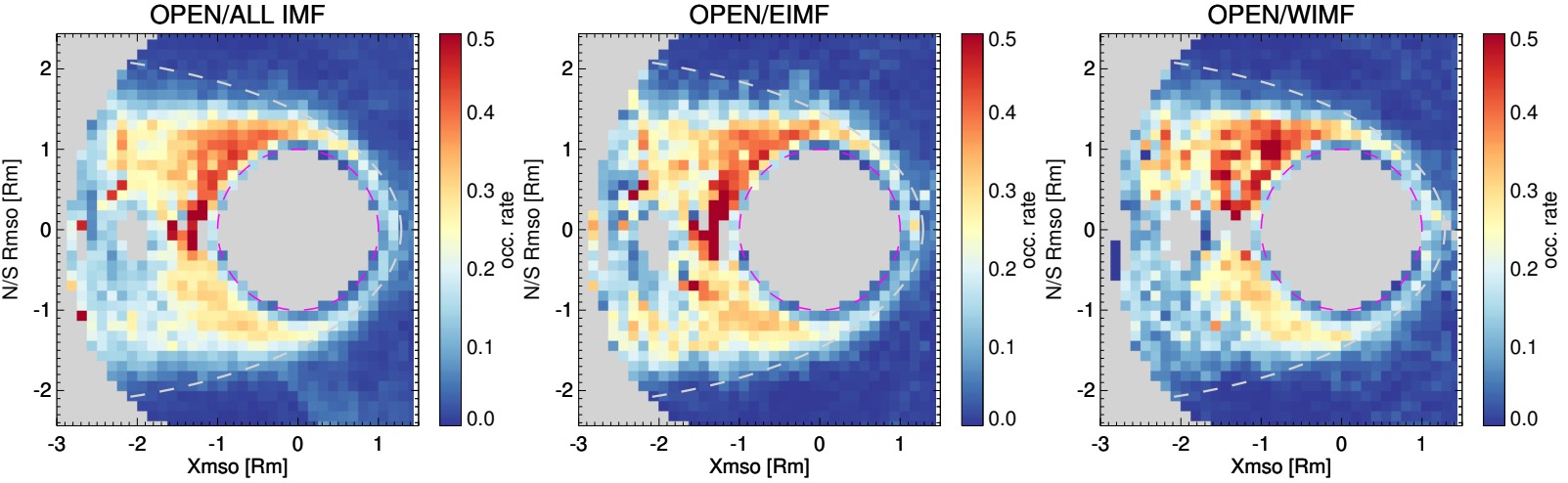
OPEN/ALL IMF
OPEN/EIMF
OPEN/WIMF
N/S Rmso [Rm]
Xmso [Rm]
occ. rate
2
1
0
-1
-2
-3
0.5
0.4
0.3
0.2
0.1
0.0